Contents lists available at ScienceDirect

Chemical Engineering Journal

journal homepage: www.elsevier.com/locate/cej

Rational design of Li off-stoichiometric Ni-rich layered cathode materials for Li-ion batteries

Seok Hyun Song [a,b], Seokjae Hong [a,b], Moses Cho [a], Jong-Gyu Yoo [c,d], Hyeong Min Jin [e], Sang-Hyuk Lee [f], Maxim Avdeev [g], Kazutaka Ikeda [h], Jongsoon Kim [i,j], Sang Cheol Nam [f], Seung-Ho Yu [b], Inchul Park [f], Hyungsub Kim [a,*]

[a] Neutron Science Division, Korea Atomic Energy Research Institute (KAERI), 111 Daedeok-daero 989 Beon-Gil, Yuseong-gu, Daejeon 34057, Republic of Korea
[b] Department of Chemical and Biological Engineering, Korea University, 145 Anam-ro, Seongbuk-gu, Seoul 02841, Republic of Korea
[c] Max Planck POSTECH/Hsinchu Center for Complex Phase Materials, 67 Cheongam-ro, Pohang 37673, Republic of Korea
[d] Department of Physics, Pohang University of Science and Technology, 67 Cheongam-ro, Pohang 37673, Republic of Korea
[e] Department of Organic Materials Engineering, Chungnam National University, Daejeon 34134, Republic of Korea
[f] LiB Materials Research Group, Secondary Battery Materials Research Laboratory, Research Institute of Industrial Science & Technology (RIST), 67 Cheongam-ro, Pohang 37673, Republic of Korea
[g] Australian Nuclear Science and Technology Organisation (ANSTO), Locked Bag 2001, Kirrawee DC, NSW 2232, Australia
[h] Institute of Materials Structure Science, High Energy Accelerator Research Organization (KEK), Tokai, Ibaraki 319-1106, Japan
[i] Department of Energy Science, Sungkyunkwan University, Suwon, 16419, Republic of Korea
[j] SKKU Institute of Energy Science and Technology (SIEST), Sungkyunkwan University, Suwon, 16419, Republic of Korea

ARTICLE INFO

ABSTRACT

The electrification trend in the automotive industry is fueling research on Ni-rich layered NCM cathode materials with high specific capacities. The simplest way to maximize the electrochemical performance of Ni-rich NCM is to tune the crystal structure by controlling the Li content and synthesis temperature. Herein, we demonstrate the critical roles of the Li content and synthesis temperature in determining the crystal structure of Li-excess Ni-rich NCM with enhanced electrochemical performance. The crystal structure of Li-excess Ni-rich NCM was systemically investigated using X-ray diffraction, neutron diffraction, and X-ray absorption spectroscopy, revealing that excess Li can be accommodated in Ni-rich NCM as the synthesis temperature decreases, resulting in stable cycle performance at high working voltage. We believe that our findings provide a rational reason for the excess amount Li required for optimization of the synthesis of Ni-rich NCM and offer insight for the simplest design of Ni-rich cathode materials that are stable under high-voltage operation.

1. Introduction

Ni-rich $LiNi_xCo_yMn_{1-x-y}O_2$ ($x \geq 0.8$) (NCM) materials are considered promising cathodes for application in electric vehicles (EVs) and grid-scale energy storage systems (ESSs) because of their high reversible capacity of over 200 mAh g^{-1} [1–3]. Nonetheless, a high Ni content in layered transition-metal (TM) oxide materials leads to serious stability issues, including i) the generation of non-stoichiometric $Li_{1-x}Ni_{1+x}O_2$ during high-temperature synthesis due to unstable trivalent nickel (Ni^{3+}), which tends to be converted into divalent nickel (Ni^{2+}); ii) oxygen release from the host structure; iii) microcracks in the bulk arising upon cycling as a result of the anisotropic lattice volume change; and iv)

the low thermal stability of the charged phases at high temperatures [4–13]. In addition, with increasing Ni content, more cation mixing between Ni ions in the TM layer and Li ions in the Li layer occurs during electrochemical cycling because of the similar ionic radii of Ni^{2+} (0.69 Å) and Li^+ (0.76 Å), and the intermixing creates a more stable insulating $Ni^{2+}O$ impurity phase on the particle surface, making the structure more unstable [14–18].

Many efforts have been focused on enhancement of the electrochemical performance of Ni-rich NCM materials through cation doping and surface coating. Doping with high-charge cations (i.e., Zr^{4+}, Nb^{5+}, and Ta^{5+}) in Ni-rich NCM materials efficiently suppresses the lattice volume change upon repeated charge/discharge processes, and the

---

uniform surface coating of NCM particles drastically reduces microstructural degradation and side reactions [19–26]. One simple approach to optimize the electrochemical performance is to change the amount of Li precursors and the synthesis temperature. Approximately 1–6 mol% excess Li precursors is commonly used for the synthesis of Ni-rich NCM materials to stabilize the trivalent nickel (Ni^{3+}) in the crystal structure and avoid the formation of the Li-deficient phase $Li_{1-x}Ni_{1+x}O_2$ [27–31]. Zhenlu *et al.* successfully synthesized $Li_{1+x}(Ni_{0.88}Mn_{0.06}Co_{0.06})_{1-x}O_2$ (x = 0–0.055) at 750 °C without impurities and demonstrated that superior electrochemical performance is achieved for a Li/TM ratio of 1.06 [27]. Eyob *et al.* also reported superior structural stability and electrochemical performance for $Li_{1+x}(Ni_{0.9}Co_{0.05}Mn_{0.05})_{1-x}O_2$ with 4% excess Li synthesized at 760 °C [31]. Li-excess Ni-rich NCM materials exhibit improved electrochemical performance; however, our understanding of why Li should be overloaded and how much Li can be incorporated into the crystalline lattice remains incomplete.

Various studies on Li- and Mn-rich layered compounds have indicated that the Li content and synthesis temperature are critical factors in determining the crystal structure and electrochemical performance [32–37]. As such, in Ni-rich NCM materials, various structural aspects depend on the amount of Li and the synthesis temperature, and the electrochemical properties of these materials are also diverse (detailed information was summarized in **Table S1**) [27–31,33,34,38–40]. Recently, Bianchini *et al.* reported the Li-excess phase of Li_2NiO_3 with high specific capacity [40]. They showed that an excess amount of Li can be incorporated into the crystal structure of $Li_{1+x}Ni_{1-x}O_2$ ($0 \leq x \leq 0.33$) at low synthesis temperatures below 600 °C, forming the $LiNiO_2$–Li_2NiO_3 solid-solution phase, similar to conventional Mn-rich Li-excess layered oxide materials. The solid solubility of Li in the crystalline lattice of Ni-rich NCM is strongly dependent on the synthesis temperature and atmosphere, which can directly affect the crystal and surface structures as well as the electrochemical performance. Furthermore, a large amount of unreacted Li source (most likely present as Li_2O) can be generated during high-temperature synthesis, and it can be transformed into LiOH or Li_2CO_3 when exposed to H_2O or CO_2 in ambient air, respectively, which requires additional washing and coating processes [19,41,42]. Therefore, understanding the crystal structure of Li-excess Ni-rich NCM and whether Li ions can be included in the TM layer or remain in the form of impurities at certain synthesis temperatures is essential.

In this study, we successfully synthesized Li-excess Ni-rich NCM materials of $Li_{(1+x)}[Ni_{0.92}Co_{0.04}Mn_{0.04}]_{(1-x)}O_2$ (x = 0.015, 0.029, 0.048, 0.074, 0.13) and unveiled the role of excess Li in the lattice upon electrochemical cycling, which differs from that in previously known Li- and Mn-rich (or Ni-rich) NCM materials. The crystal and surface structures of $Li_{(1+x)}[Ni_{0.92}Co_{0.04}Mn_{0.04}]_{(1-x)}O_2$ were systematically investigated using X-ray diffraction (XRD), neutron diffraction (ND), and X-ray absorption spectroscopy (XAS) analyses, revealing that excess Li can be incorporated into the TM layer at a relatively low synthesis temperature of 750 °C or 700 °C in the form of $LiMO_2$ (*R-3 m*) or Li_2MO_3 (*C2/m*). Excess Li ions located in the TM layer serve as a structural stabilizer during charging and discharging with low and high cut-off voltages (i.e., 4.25 and 4.5 V), enhancing the cycle stability. We believe that our findings will shed light on optimization of the synthesis of Li- and Ni-rich layered cathode materials while maximizing their electrochemical performance with a highly stabilized redox reaction under high-voltage operation.

2. Experimental section

2.1. Synthesis of Li$_{(1+x)}$[Ni$_{0.92}$Co$_{0.04}$Mn$_{0.04}$]$_{(1-x)}$O$_2$

$Li_{(1+x)}[Ni_{0.92}Co_{0.04}Mn_{0.04}]_{(1-x)}O_2$ (x = 0.015, 0.029, 0.048, 0.074, 0.13) powder samples were synthesized using a conventional solid-state method. A stoichiometric amount of $(1+x)$LiOH·H_2O (99.995%, Sigma-Aldrich) and $(1-x)Ni_{0.92}Co_{0.04}Mn_{0.04}(OH)_2$ were carefully mixed by hand grinding to prevent particle breakage, and the ground powder was pelletized under a pressure of 250 kg cm^{-2}. The mixture pellets were calcinated at different temperatures of 800 °C, 750 °C, and 700 °C for 12 h under O_2 gas flow. The O_2 gas flow rate was 400–500 cc min^{-1}. The resulting powder was collected from the furnace at 120 °C and stored in an Ar-filled glove box to avoid moisture exposure. To clarify the correlation of the Li and TM ratio, the nominal ratios between LiOH·H_2O and $Ni_{0.92}Co_{0.04}Mn_{0.04}(OH)_2$ were set as 1.03:1 (x = 0.015), 1.06:1 (x = 0.029), 1.10:1 (x = 0.048), 1.16:1 (x = 0.074), and 1.30:1 (x = 0.13) for the synthesis of $Li_{(1+x)}[Ni_{0.92}Co_{0.04}Mn_{0.04}]_{(1-x)}O_2$.

2.2. Structure characterization of Li$_{(1+x)}$[Ni$_{0.92}$Co$_{0.04}$Mn$_{0.04}$]$_{(1-x)}$O$_2$

The crystal structure of the $Li_{(1+x)}[Ni_{0.92}Co_{0.04}Mn_{0.04}]_{(1-x)}O_2$ powder samples was characterized using XRD and ND analyses. Powder XRD data were obtained using an X-ray diffractometer (Empyrean, Malvern PANalytical) equipped with Cu Kα$_1$ radiation (λ = 1.540598 Å). The measurement was performed in the 2θ range of 10°–90° with a step size of 0.013° and step time of 1 s. *In situ* charge/discharge XRD data were collected in the 2θ range of 10°–70° with a step size of 0.026° and step time of 0.3 s. The measurement was conducted using specially designed Swagelok-type cells with beryllium windows. Synchrotron XRD experiments of $Li_{(1+x)}[Ni_{0.92}Co_{0.04}Mn_{0.04}]_{(1-x)}O_2$ (x = 0.13) samples synthesized at 800 °C (E5) and 700 °C (H-E5) were performed at BL9B beamline at Pohang Accelerator Laboratory (PAL). ND data of $Li_{(1+x)}[Ni_{0.92}Co_{0.04}Mn_{0.04}]_{(1-x)}O_2$ were obtained using Echidna machine at the OPAL facilities of the Australian Nuclear Science and Technology Organization (ANSTO). ND data were collected in the 2θ range of 0–163.95° with a step size of 0.05 using a constant wavelength of 1.6215 Å. The local structural analysis of $Li_{(1+x)}[Ni_{0.92}Co_{0.04}Mn_{0.04}]_{(1-x)}O_2$ was conducted using neutron total scattering spectrometer (NOVA, beamline BL21 at the 90° (Q (=2π/d = 4πsinθ/λ) detector bank) at Japan Proton Accelerator Research Complex (J-PARC). Neutron pair distribution function (PDF) analysis (PDFgui) was performed for both PDFs *G(r)* Fourier transformed from the synchrotron and neutron total scattering data [43]. The valence states of Ni, Co, and Mn were characterized XAS at beamlines of 7D (XAFS), 8C (Nano XAFS), and 6A (MPK MEXIM) at the Pohang Acceleratory Laboratory (PAL). XAS data around the Ni K-edge, Ni L-edge, Co L-edge, and Mn L-edge were obtained in transmission mode using an electron energy of 3 GeV and a current of 400 mA. The particle morphology of 50 cycled samples of $Li_{(1+x)}[Ni_{0.92}Co_{0.04}Mn_{0.04}]_{(1-x)}O_2$ (x = 0, 0.029) synthesized at 750 °C was characterized using Scanning Electron Microscope (SEM) (S-4800, Hitachi). The cross-section image was obtained from the sample by Focused Ion Beam (FIB)-SEM (Helios Nanolab 450 F1) at KAIST Analysis Center for Research Advancement (KARA).

2.3. Washing process of Li$_{(1+x)}$[Ni$_{0.92}$Co$_{0.04}$Mn$_{0.04}$]$_{(1-x)}$O$_2$

0.5 g of $Li_{(1+x)}[Ni_{0.92}Co_{0.04}Mn_{0.04}]_{(1-x)}O_2$ were mixed with 2.5 ml of ethanol (99.99%, Sigma-Aldrich) with 0.04 g of H_3BO_3, and stirred with 700 rpm for 5 min. The solution was filtered, and the resulting powder was dried at 110 °C for 2 h under vacuum, followed by heating at 400 °C for 4 h under O_2 gas flowing.

2.4. Electrochemical analyses of Li$_{(1+x)}$[Ni$_{0.92}$Co$_{0.04}$Mn$_{0.04}$]$_{(1-x)}$O$_2$

The electrodes were prepared using $Li_{(1+x)}[Ni_{0.92}Co_{0.04}Mn_{0.04}]_{(1-x)}O_2$, Super P, and polyvinylidene fluoride (PVDF) binder in a mass ratio of 92:4:4 in N-methyl-2-pyrrolidone (99.5%, Aldrich). The resulting slurry was coated to 250-μm thickness onto aluminum foil, vacuum dried, and roll pressed. The mass loading of the active material in each electrode was 4.6–5.7 mg cm^{-2}. Li foil was used as the counter and reference electrode. Coin-type half cells (CR2032, Wellcos) were assembled using the electrode, a lithium metal counter electrode, a glass microfiber filter (grade GF/F, Whatman) as a separator, and 1 M LiPF$_6$ in

ethylene carbonate/dimethyl carbonate (EC/DMC, 1:1 v/v, PanaXEtec) as the electrolyte. The preparation was conducted in an Ar-filled glovebox. Galvanostatic charge/discharge measurements of the $Li_{(1+x)}[Ni_{0.92}Co_{0.04}Mn_{0.04}]_{(1-x)}O_2$ electrode samples were performed in the voltage ranges of 2.5–4.25 V and 2.5–4.5 V *vs.* Li^+/Li with a constant current of 40 mA g^{-1} and 200 mA g^{-1}, each equivalent to 0.15C-rate and 1C-rate at 25 °C, respectively (WBCS 3000, WonA Tech).

3. Results and discussion

3.1. Synthesis and structural characterization of $Li_{(1+x)}[Ni_{0.92}Co_{0.04}Mn_{0.04}]_{(1-x)}O_2$

Fig. 1a presents XRD patterns of $Li_{(1+x)}[Ni_{0.92}Co_{0.04}Mn_{0.04}]_{(1-x)}O_2$ (x = 0.015, 0.029, 0.048, 0.074, 0.13) synthesized at 800 °C, 750 °C, and 700 °C. The corresponding samples were designated as E1 to 5, M−E1 to 5, and H-E1 to 5, respectively, depending on the Li content and synthesis temperature. The nominal ratios between LiOH·H_2O and $Ni_{0.92}Co_{0.04}Mn_{0.04}(OH)_2$ were set at 1.03:1 (x = 0.015), 1.06:1 (x = 0.029), 1.10:1 (x = 0.048), 1.16:1 (x = 0.074), and 1.30:1 (x = 0.13) for the synthesis of $Li_{(1+x)}[Ni_{0.92}Co_{0.04}Mn_{0.04}]_{(1-x)}O_2$, where x means the target Li content, not the composition of the real sample, detailed information was covered in a later section. All the diffraction peaks can be readily indexed to the hexagonal structure (*R-3 m*) of $LiNiO_2$. No trace of impurities for x = 0.015 was observed for any of the samples, and the different peak intensities were assigned to Li_2O, Li_2CO_3, and *C2/m* Li_2MO_3 phases depending on the Li composition and synthesis temperature. Impurity peaks of Li_2O and Li_2CO_3 began to appear when the Li content reached ∼ 3% (x = 0.029) for the series of E1 to 5 samples synthesized at 800 °C and increased with increasing Li content. Fewer impurity peaks were observed for the powder samples synthesized at the lower temperature of 750 °C, and there was no trace of impurity phases in the 700 °C samples, indicating the presence of the solid-solution phase $Li_{(1+x)}[Ni_{0.92}Co_{0.04}Mn_{0.04}]_{(1-x)}O_2$. Note that weak broad peaks near 22°, which can be indexed as the (020) and (110) planes of the monoclinic structure (*C2/m*, Li_2MO_3), were observed for H-E5, as shown in the inset of Fig. 1a and **Fig. S1**. From these results, it can be observed that with decreasing synthesis temperature, more Li can be incorporated into the hexagonal structure (*R-3 m*), and the Li transforms into the $LiMO_2$–Li_2MO_3 phase with Li–Ni ordering in the TM layer when the Li content reaches x = 0.13. Fig. 1b shows the quantitative amount of Li_2O and Li_2CO_3 impurities analyzed by Rietveld refinement of the XRD patterns. Approximately 1.49 wt% of the Li_2O phase was evolved from the E2 sample, with this amount gradually increasing as the Li content increased to x = 0.13 (E5), reaching 5.31 wt%. A smaller amount (∼2 wt%) of Li_2O was observed for the M−E1 to 5 samples synthesized at 750 °C, and no impurity phase was detected for the H-E1 to 5 samples.

The lattice parameter and unit-cell volume of $Li_{(1+x)}[Ni_{0.92}Co_{0.04}Mn_{0.04}]_{(1-x)}O_2$ were further characterized to confirm whether the excess Li resides in the crystalline lattice, as shown in Fig. 1c and Fig. S2–S3. Negligible *a*- and *c*-lattice and unit-cell volume changes (<0.2%) were observed for the E1 to 5 samples with increasing Li content. For the M−E1 to 5 samples synthesized at the lower temperature of 750 °C, the unit-cell volume decreased from 101.401 (1) to 100.634 (1) Å^3 as the Li content increased, indicating a volume change of ∼ 0.75%. Note that the largest volume change (∼1.59%) was confirmed for the H-E1 to 5 samples, indicating that the largest Li content can be accommodated in the lattice of $Li_{(1+x)}[Ni_{0.92}Co_{0.04}Mn_{0.04}]_{(1-x)}O_2$. The significant decrease of the cell parameters of H-E1 to 5 is attributed to the increase of the oxidation state of the TM for charge compensation, shortening the bond length between the TM and oxygen ions. The atomic disorder or lattice strain in $Li_{(1+x)}[Ni_{0.92}Co_{0.04}Mn_{0.04}]_{(1-x)}O_2$ was further characterized using a Williamson–Hall (W–H) plot, as shown in **Fig. S4**. The slope of the W–H plot increased as the synthesis temperature decreased from 800 °C to 700 °C and the Li content increased, indicating an increase of microstrain or structural disorder in $Li_{(1+x)}[Ni_{0.92}Co_{0.04}Mn_{0.04}]_{(1-x)}O_2$. From these results, it is expected that as the synthesis temperature decreases and the Li content increases, more atomic disorder is present in the structure. Detailed structural information obtained from Rietveld refinement of the XRD patterns is presented in the Supporting Information (**Fig. S5–7** and **Tables S2–4**).

To quantify the atomic structural parameters of $Li_{(1+x)}[Ni_{0.92}Co_{0.04}Mn_{0.04}]_{(1-x)}O_2$, ND experiments were conducted. The ND patterns in Fig. 2a indicate that all the reflection peaks can be well assigned to the hexagonal structure (*R-3 m*) with a trace amount of Li_2O and Li_2CO_3 impurity phases, consistent with the XRD results. The atomic positions
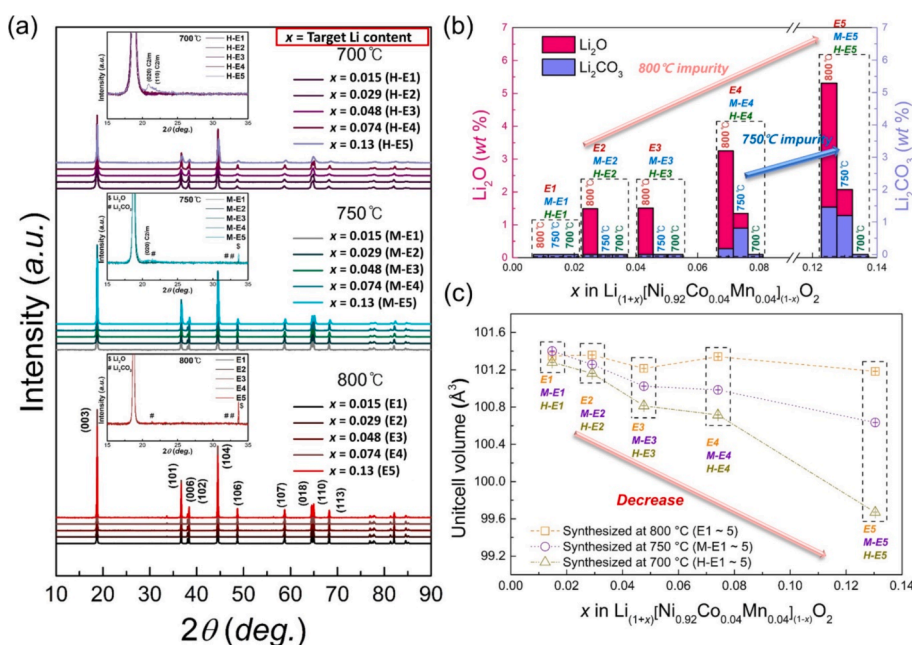
Fig. 1. (a) X-ray diffraction (XRD) patterns of $Li_{(1+x)}[Ni_{0.92}Co_{0.04}Mn_{0.04}]_{(1-x)}O_2$ (x = 0.015, 0.029, 0.048, 0.074, 0.13) synthesized at 800 °C, 750 °C, and 700 °C. (b) Weight fraction of impurity phases of Li_2O and Li_2CO_3 from Rietveld refinement of XRD patterns. (c) Unit-cell volume changes of $Li_{(1+x)}[Ni_{0.92}Co_{0.04}Mn_{0.04}]_{(1-x)}O_2$ at 800 °C, 750 °C, and 700 °C.

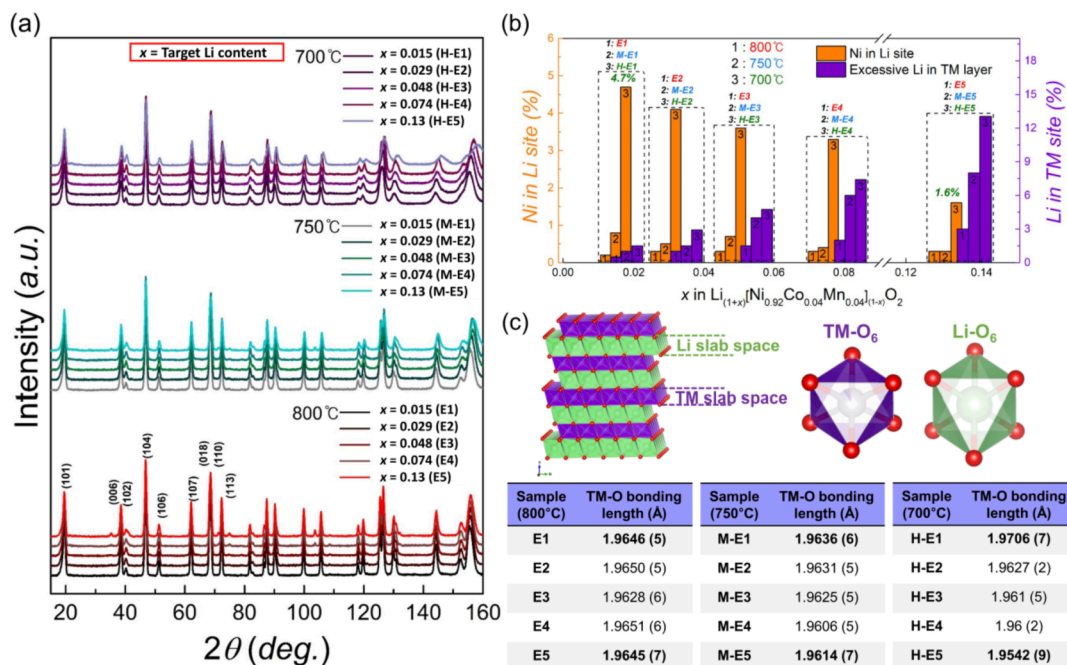**Fig. 2.** (a) Neutron diffraction (ND) patterns of $Li_{(1+x)}[Ni_{0.92}Co_{0.04}Mn_{0.04}]_{(1-x)}O_2$ (x = 0.015, 0.029, 0.048, 0.074, 0.13) synthesized at 800 °C, 750 °C, and 700 °C. (b) Percent of Ni in the Li layer and excess Li content in the TM layer obtained from Rietveld refinement of the ND patterns. (c) TM–O bond length $Li_{(1+x)}[Ni_{0.92}Co_{0.04}Mn_{0.04}]_{(1-x)}O_2$ (x = 0.015, 0.029, 0.048, 0.074, 0.13) synthesized at 800 °C, 750 °C, and 700 °C.

and occupancies were analyzed by Rietveld refinement, as shown in **Fig. S8–10** and **Tables S5–7**. The fitting was satisfactory with low reliability factors. Fig. 2b shows the quantitative amount of Ni in the Li layer and excess Li in the TM layer of $Li_{(1+x)}[Ni_{0.92}Co_{0.04}Mn_{0.04}]_{(1-x)}O_2$ synthesized at 800 °C, 750 °C, and 700 °C. A comparably large amount (>3.0%) of Ni in the octahedral sites in the Li layer (Li_{oct}) was observed for the samples synthesized at 700 °C (H-E1 to 4), whereas negligible Ni in Li_{oct} (<1%) was observed for the samples synthesized at 750 °C and 800 °C (E1 to 5 and M–E1 to 5). As the synthesis temperature and Li content decreased, more Ni^{2+} cations were present in the lattice, which may have resulted from the insufficient oxidation of Ni in $Li_{(1+x)}[Ni_{0.92}Co_{0.04}Mn_{0.04}]_{(1-x)}O_2$ during the synthesis process [44–46]. Unlike the Ni migration to Li_{oct}, the excess amount of Li in the TM layer increased as the synthesis temperature decreased from 800 °C to 700 °C (as indicated by the purple bars). Approximately 3% excess Li was detected in the lattice in E5 for the target Li content of x = 0.13. The remaining Li reacted with O_2 and CO_2, forming Li_2O and Li_2CO_3 impurity phases, respectively. A maximum 8% of Li resided in the TM layer when the target Li content was x = 0.13 at the synthesis temperature of 750 °C. Unlike the E1 to 5 and M–E1 to 5 samples, all of the target contents of Li were incorporated into the crystal structure of $Li_{(1+x)}[Ni_{0.92}Co_{0.04}Mn_{0.04}]_{(1-x)}O_2$ (H-E1 to 5), where ~ 13% excess Li was detected for the H-E5 (x = 0.13) sample. This result indicates that a large amount of Li can substitute for the TMs in the TM layer during low-temperature synthesis. In addition, a large amount of Li located in the TM layer leads to in-plane Li–Ni ordering, forming the $C2/m$ structure, which is consistent with previous reports [38,40].

Fig. 2c presents the TM–O bond lengths of the TMO_6 octahedra in $Li_{(1+x)}[Ni_{0.92}Co_{0.04}Mn_{0.04}]_{(1-x)}O_2$ synthesized at 800 °C, 750 °C, and 700 °C. Note that the largest TM–O bond-length change was confirmed from the H-E1 to 5 samples synthesized at 700 °C, where the TM–O bond length decreased from 1.9706 (7) Å to 1.9542 (9) (~0.8%) and the TM slab space decreased from 2.1365 (5) Å to 2.1014 (8) Å (~1.7%), whereas a negligible change was observed for the E1 to 5 and M–E1 to 5 samples, which is in good agreement with the change of the cell parameters and unit-cell volume. These results confirm that as the synthesis temperature decreases, the excess Li ions are more likely to be

located in the TM layer, resulting in an increase of the oxidation state of TMs and a decrease of the TM–O bond lengths. A detailed comparison of the TM–O and Li–O bond lengths and slab space of the samples with different Li contents and synthesis temperatures is presented in **Table S8**.

3.2. Valence state and local structure analyses of $Li_{(1+x)}[Ni_{0.92}Co_{0.04}Mn_{0.04}]_{(1-x)}O_2$

The oxidation states of Ni in $Li_{(1+x)}[Ni_{0.92}Co_{0.04}Mn_{0.04}]_{(1-x)}O_2$ were examined using X-ray absorption near-edge structure (XANES) analysis, as shown in Fig. 3a–c. The Ni K-edge XANES spectra of $Li_{(1+x)}[Ni_{0.92}Co_{0.04}Mn_{0.04}]_{(1-x)}O_2$ synthesized at 800 °C, 750 °C, and 700 °C show a spectral shift to higher energies as the amount of Li increases from x = 0.015 to 0.13. Note that the largest shift of 0.8 eV was confirmed for the H-E1 to 5 series samples, whereas a negligible energy shift was observed for the E1 to 5 samples. An energy shift of approximately 0.4 eV was confirmed for the M−E1 to 5 samples. **Fig. S11a** shows the apparent shift of the edge position to the higher-energy region as the synthesis temperature decreases from 800 °C to 700 °C for a Li content of x = 0.13, which indicates the Ni oxidation in $Li_{(1+x)}[Ni_{0.92}Co_{0.04}Mn_{0.04}]_{(1-x)}$ occurs due to Li substitution on TM sites at lower synthesis temperature with high Li content. However, interestingly, when the Li content decreased to x = 0.015, the oxidation state of Ni in $Li_{(1+x)}[Ni_{0.92}Co_{0.04}Mn_{0.04}]_{(1-x)}O_2$ with the 700 °C synthesis condition was lower than that in samples synthesized at 800 °C and 750 °C due to the presence of more Ni^{2+} cations in Li layer, which shows the strong correlation to is ND results. This means that a layered structure with a large amount of Li/Ni cation mixing can be formed in the lower synthesis temperature at lower Li content [44–46]. The effect of excess Li on the oxidation state of Ni and the local structure of $Li_{(1+x)}[Ni_{0.92}Co_{0.04}Mn_{0.04}]_{(1-x)}O_2$ was further characterized using neutron PDF analysis, as presented in **Fig. S12**. The results reveal that the amount of Jahn–Teller-active Ni^{3+} increased as the Li content increased in $Li_{(1+x)}[Ni_{0.92}Co_{0.04}Mn_{0.04}]_{(1-x)}O_2$ synthesized at 800 °C and 750 °C due to the oxidation of Ni from Ni^{2+} to Ni^{3+}, whereas it decreased in the sample synthesized at 700 °C due to the decrease of Ni^{3+} and increase of Ni^{4+}. A detailed
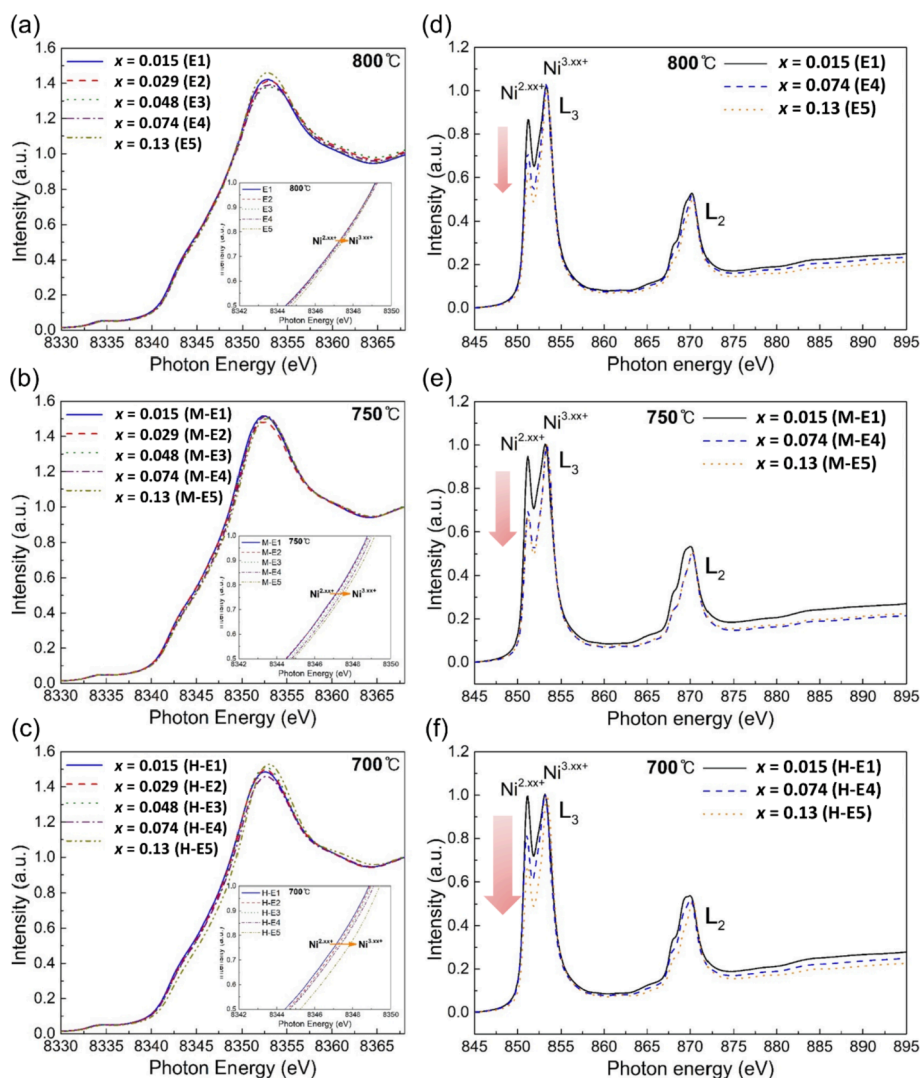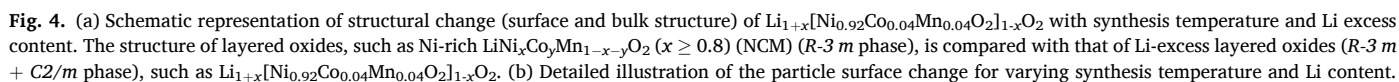
Fig. 3. Ni K-edge X-ray absorption near edge structure (XANES) spectra of $Li_{(1+x)}[Ni_{0.92}Co_{0.04}Mn_{0.04}]_{(1-x)}O_2$ ($x = 0.015, 0.029, 0.048, 0.074, 0.13$) synthesized at (a) 800 °C, (b) 750 °C, and (c) 700 °C. Ni L-edge X-ray absorption spectroscopy (XAS) spectra of $Li_{(1+x)}[Ni_{0.92}Co_{0.04}Mn_{0.04}]_{(1-x)}O_2$ ($x = 0.015, 0.029, 0.048, 0.074, 0.13$) synthesized at (d) 800 °C, (e) 750 °C, and (f) 700 °C.

comparison of the samples for varying Li content and synthesis temperature is presented in **Fig. S13**.

The oxidation states of Ni, Co, and Mn on the particle surface were characterized using soft XAS. The soft XAS data were collected using the total electron yield (TEY) mode to obtain information on the oxidation state on the particle surface (10 nm). Fig. 3d–f presents the Ni L_2- and L_3-edge XAS spectra of $Li_{(1+x)}[Ni_{0.92}Co_{0.04}Mn_{0.04}]_{(1-x)}O_2$ ($x = 0.015, 0.074,$ and 0.13) synthesized at 800 °C, 750 °C, and 700 °C. The results indicate that the oxidation state of Ni on the particle surface of $Li_{(1+x)}[Ni_{0.92}Co_{0.04}Mn_{0.04}]_{(1-x)}O_2$ is mainly composed of Ni^{3+} with a small amount of Ni^{2+} [47–50]. Note that more Ni^{2+} was detected for H-E1 than for M−E1 and E1 (**Fig. S14a**), whereas a negligible difference in the oxidation state of Ni was observed for the XANES analysis, suggesting a high probability of the presence of Ni^{2+} on the particle surface. The Ni^{2+} may have originated from the preferential migration of Ni from the TM layer to the Li layer on the surface of the materials and resulting formation of Ni^{2+}–O rock-salt phases [16]. The intensity of the first peak (851.2 eV) at the Ni L_3-edge showed a decreasing tendency as the Li content increased, regardless of the synthesis temperature, indicating the increase of the oxidation state of Ni from 2 + to 3 + or 4 +. Interestingly, almost the same peak intensity of the Ni L_3-edge was confirmed from the samples with a Li content of $x = 0.13$ (E5, M−E5, and H-E5), as shown in
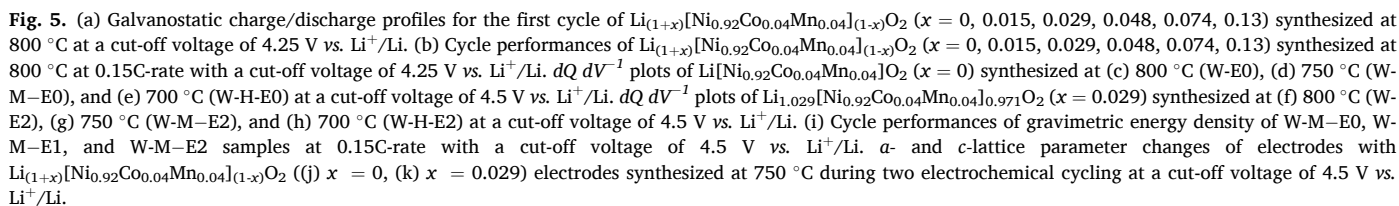
Fig. S14b, indicating that the largest oxidation-state change occurred for the samples synthesized at 700 °C. This result confirmed that the largest amount of Li was inserted into the TM layer during synthesis at 700 °C, which is consistent with the XANES, ND, and PDF results. There was no change in the oxidation states of Co and Mn on the particle surface of $Li_{(1+x)}[Ni_{0.92}Co_{0.04}Mn_{0.04}]_{(1-x)}O_2$ ($x = 0.015, 0.074, 0.13$), as shown in **Fig. S15**.

A schematic representation of the structural changes of as-synthesized $Li_{(1+x)}[Ni_{0.92}Co_{0.04}Mn_{0.04}]_{(1-x)}O_2$ depending on the synthesis temperature and Li target content is presented in Fig. 4, detailed information for the real Li content and weight fraction of impurity phases upon target Li content was denoted in **Table S9**. Through the simple characterization of as-prepared samples, we demonstrated that appropriate control of the synthesis temperature and Li content is required when synthesizing Ni-rich NCM materials. As the synthesis temperature decreased from 800 °C to 750 °C and 700 °C, the amount of Ni^{2+} ions gradually increased, and at the same time, as the Li content increased, it was confirmed that Li^+ ions took the place of Ni^{2+} ions. A highly crystalline layer structured phase of $Li_{(1+x)}[Ni_{0.92}Co_{0.04}Mn_{0.04}]_{(1-x)}O_2$ with low Li–Ni intermixing was successfully synthesized at a synthesis temperature of 800 °C; however, a large amount of impurities such as Li_2O and Li_2CO_3 were formed on the particle surface

Fig. 4. (a) Schematic representation of structural change (surface and bulk structure) of $Li_{1+x}[Ni_{0.92}Co_{0.04}Mn_{0.04}O_2]_{1-x}O_2$ with synthesis temperature and Li excess content. The structure of layered oxides, such as Ni-rich $LiNi_xCo_yMn_{1-x-y}O_2$ ($x \geq 0.8$) (NCM) (*R-3 m* phase), is compared with that of Li-excess layered oxides (*R-3 m* + *C2/m* phase), such as $Li_{1+x}[Ni_{0.92}Co_{0.04}Mn_{0.04}O_2]_{1-x}O_2$. (b) Detailed illustration of the particle surface change for varying synthesis temperature and Li content.

even when the excess amount of Li was very small. Less impurities were evolved from the samples synthesized at 750 °C due to the increased amount of Li insertion into the hexagonal lattice. At the lowest synthesis temperature of 700 °C, the crystallinity was the lowest; however, more Li was incorporated into the lattice, forming the $LiMO_2$–Li_2MO_3 phase with Li–Ni ordering in the TM layer without impurities.

3.3. Electrochemical performance of $Li_{(1+x)}[Ni_{0.92}Co_{0.04}Mn_{0.04}]_{(1-x)}O_2$

To investigate the effect of excess Li in the crystalline lattice on the electrochemical performance, galvanostatic charge/discharge tests of $Li_{(1+x)}[Ni_{0.92}Co_{0.04}Mn_{0.04}]_{(1-x)}O_2$ ($x = 0$, 0.015, 0.029, 0.048, 0.074, 0.13) were conducted. The electrode was fabricated with 94% active

Fig. 5. (a) Galvanostatic charge/discharge profiles for the first cycle of $Li_{(1+x)}[Ni_{0.92}Co_{0.04}Mn_{0.04}]_{(1-x)}O_2$ ($x = 0$, 0.015, 0.029, 0.048, 0.074, 0.13) synthesized at 800 °C at a cut-off voltage of 4.25 V *vs.* Li^+/Li. (b) Cycle performances of $Li_{(1+x)}[Ni_{0.92}Co_{0.04}Mn_{0.04}]_{(1-x)}O_2$ ($x = 0$, 0.015, 0.029, 0.048, 0.074, 0.13) synthesized at 800 °C at 0.15C-rate with a cut-off voltage of 4.25 V *vs.* Li^+/Li. $dQ\ dV^{-1}$ plots of $Li[Ni_{0.92}Co_{0.04}Mn_{0.04}]O_2$ ($x = 0$) synthesized at (c) 800 °C (W-E0), (d) 750 °C (W-M−E0), and (e) 700 °C (W-H-E0) at a cut-off voltage of 4.5 V *vs.* Li^+/Li. $dQ\ dV^{-1}$ plots of $Li_{1.029}[Ni_{0.92}Co_{0.04}Mn_{0.04}]_{0.971}O_2$ ($x = 0.029$) synthesized at (f) 800 °C (W-E2), (g) 750 °C (W-M−E2), and (h) 700 °C (W-H-E2) at a cut-off voltage of 4.5 V *vs.* Li^+/Li. (i) Cycle performances of gravimetric energy density of W-M−E0, W-M−E1, and W-M−E2 samples at 0.15C-rate with a cut-off voltage of 4.5 V *vs.* Li^+/Li. *a*- and *c*-lattice parameter changes of electrodes with $Li_{(1+x)}[Ni_{0.92}Co_{0.04}Mn_{0.04}]_{(1-x)}O_2$ ((j) $x = 0$, (k) $x = 0.029$) electrodes synthesized at 750 °C during two electrochemical cycling at a cut-off voltage of 4.5 V *vs.* Li^+/Li.

material with high mass loading (~5 mg cm^{-2}). For the clear comparison of the electrochemical performances, washing and heating processes of Li-excess samples were performed to eliminate the residual Li compounds [42,51]. There was no trace of impurity after washing and heating, as shown in **Fig. S16**. Fig. 5a presents the galvanostatic charge/discharge profiles for the first cycle of Li$_{(1+x)}$[Ni$_{0.92}$Co$_{0.04}$Mn$_{0.04}$]$_{(1-x)}$O$_2$ synthesized at 800 °C at 0.15C-rate with a cut-off voltage of 4.25 V. A discharge capacity of 217 mAh g^{-1} was delivered from stoichiometric LiNi$_{0.92}$Co$_{0.04}$Mn$_{0.04}$O$_2$ (W-E0), and it decreased to 190 mAh g^{-1} as the target Li content increased from 1 to 1.13. The largest decrease of initial discharge capacity was observed from the sample synthesized at 700 °C, as presented in **Fig. S17b**, where the initial discharge capacity of 184 mAh g^{-1} was obtained from the stoichiometric sample (W-H-E0), and it decreased to 112 mAh g^{-1} when the target Li content approached 1.13. The rational reason for the larger decrease in the initial discharge capacity from the W-H-E0 to 5 and W-M−E0 to 5 samples than from the W-E0 to 5 sample is the reduction of the Ni content and increase of the Ni oxidation state due to the increased Li insertion in the TM layer. The charge/discharge capacities and Coulombic efficiency during the initial cycle are presented in **Table S10**. A similar trend was observed for all the Li-excess electrodes when the cut-off voltage was 4.5 V, with the largest decrease in the initial discharge capacity observed from the W-H-E0 to 5 samples due to the large Li insertion (see **Fig. S18** and **Table S11**). Note that a significant change in the initial charge profile was observed for W-H-E4 and W-H-E5, where a long slope plateau was observed in the voltage range of 4.3–4.5 V. This profile change is attributed to the in-plane ordering between Li and Ni in the TM layer, leading to the oxygen oxidation reaction, as reported by Kyojin et al and Bianchini et al [37,40]. The electrode delivered a high charge capacity of 250 mAh g^{-1}; however, only 55% of the capacity (139 mAh g^{-1}) was reversible for W-H-E5 upon the following discharge process. The highly reactive oxidized oxygen may react with the electrolyte, resulting in outgassing of O$_2$ and CO$_2$ and the formation of an unfavorable cathode–electrolyte interphase and rock-salt phase (Ni^{2+}–O) on the particle surface, leading to deterioration of the electrochemical performance.

The cycle performance of Li$_{(1+x)}$[Ni$_{0.92}$Co$_{0.04}$Mn$_{0.04}$]$_{(1-x)}$O$_2$ synthesized at 800 °C (W-E0 to 5) at 0.15C-rate with a cut-off voltage of 4.25 V *vs.* Li$^+$/Li is shown in **Fig. 5b**. W-E1 with a target Li content of 1.015 exhibited the most stable capacity retention of 194 mAh g^{-1} (96 %) after 50 cycles, whereas 187 mAh g^{-1} (88%) was maintained from W-E0. More Li in TM layer resulted in an overall improved capacity retention for all the Li-excess samples (W-M−E0 to 5 and W-H-E0 to 5), whereas they suffered from the low initial discharge capacities (see **Fig. S19**). To further verify the efficacy of excess Li in the TM layer, the cycle performances of Li$_{(1+x)}$[Ni$_{0.92}$Co$_{0.04}$Mn$_{0.04}$]$_{(1-x)}$O$_2$ (x = 0, 0.015, 0.029, 0.048, 0.074, 0.13) was examined at 0.15C-rate with a high cut-off voltage of 4.5 V *vs.* Li$^+$/Li. The Li-excess samples synthesized at 800 °C and 750 °C exhibited enhanced capacity retention, and the best capacity retention was confirmed from W-M−E2 synthesized at 750 °C with a target Li content of 1.029, as shown in **Fig. S20a and b**. A discharge capacity of approximately 198 mAh g^{-1} (93%) was maintained after 50 cycles from W-M−E2; in contrast, the stoichiometric sample (W-M−E0) exhibited a significant capacity decay with 78% retention (see **Table S12**). The improved capacity retention may be attributed to the excess Li in the TM layer, stabilizing the crystal structure during electrochemical cycling. It should be noted that the superior cycle performance at high voltage was obtained through simple Li composition and synthesis temperature changes without coating or the use of electrolyte additives. Interestingly, the poor cycle performance of W-H-E1 to 5 was confirmed at a high cut-off voltage of 4.5 V, which was assumed to be caused by an irreversible oxygen redox reaction, as shown in **Fig. S20c** [40]. The stoichiometric sample (W-H-E0) presented high capacity retention of 98% after 50 cycles at 4.5 V, whereas Li-excess sample (W-H-E5) showed a prominent capacity decay with 83% retention, with the detailed information exhibited in **Table S12**. Li-excess samples also showed overall improved capacity

retention during 150 cycles at a high current rate of 1C-rate, as presented in **Fig. S21**. Fig. 5c–h present *dQ dV^{-1}* plots of Li$_{(1+x)}$[Ni$_{0.92}$Co$_{0.04}$Mn$_{0.04}$]$_{(1-x)}$O$_2$ (x = 0, 0.029) at a cut-off voltage of 4.5 V. The well-known sequential phase transition (H1–M−H2–H3) for Ni-rich NCM materials was observed for all the samples. A significant voltage decay was observed from stoichiometric compounds of LiNi$_{0.92}$Co$_{0.04}$Mn$_{0.04}$O$_2$ (**Fig. 5c–e**), where overpotentials of 0.33, 0.21, and 0.13 V were confirmed for W-E0, W-M−E0, and W-H-E0, respectively. This is consistent with our previous results that high-voltage operation of a Ni-rich NCM electrode accelerates the voltage decay originating from the formation of the Ni^{2+}–O rock-salt phase on the particle surface [16]. Notably, the Li-excess electrodes showed less voltage decay than stoichiometric compounds upon repeated electrochemical cycling, as illustrated in **Fig. 5f–h**. W-E2, W-M−E2, and W-H-E2 showed a low overpotential of 0.18, 0.13, and 0.11 V after 50 cycles, respectively. Benefiting from improved capacity and voltage retentions, approximately 91% of the energy density was maintained after 50 cycles for W-M−E2, as shown **Fig. 5i**.

To understand the structural evolution upon electrochemical cycling, *in situ* XRD analyses of Li$_{(1+x)}$[Ni$_{0.92}$Co$_{0.04}$Mn$_{0.04}$]$_{(1-x)}$O$_2$ (x = 0 and 0.029) was conducted. **Fig. S22** presents *in situ* XRD patterns of W-M−E0 and W-M−E2 during charge/discharge processes with a cut-off voltage of 4.5 V *vs.* Li$^+$/Li. The (0 0 3) peak underwent a continuous peak shift to lower 2θ angle during the initial charge process until 4.0 V, followed by shifting toward higher 2θ angle up to 4.5 V. In addition, the reversible H1–M−H2–H3 structural transition during charging and discharging was confirmed until the 2nd cycles, which is consistent with previous findings [9,16,52,53]. The *a*- and *c*-lattice parameter changes of W-M−E0 during initial charging and discharging are presented in **Fig. 5j**. A continuous change of the *a*- and *c*-lattice parameters was observed during charging up to 4.0 V, and a notable lattice parameter change was observed in the highly delithiated state above 4.0 V, where a large contraction of the *c*-lattice (5.2%) occurred during charging from 4.0 to 4.5 V due to the phase transition from H2 to H3. Note that less lattice parameter change was confirmed for the W-M−E2 during charging and discharging, as shown in **Fig. 5k**. Approximately 4.5% of *c*-lattice contraction was confirmed during charging up to 4.5 V, and it was maintained to the second cycle. We believe that the improved cycle stability at high voltage is mainly due to the immobile Li in the TM layer, which stabilized the crystal structure with a small lattice expansion/contraction during electrochemical cycling. The change of particle morphology after electrochemical cycling at a cut-off voltage of 4.5 V was further characterized by FIB-SEM analysis, as shown in **Fig. S23–24**. Results revealed that Li-excess sample of W-M−E2 maintained its particle morphology with less microcrack formation after 50 cycle of charge/discharge than W-M−E0.

3.4. New insight into synthesis and engineering of Ni-rich NCM

Results of our study indicate the importance of controlling the Li content according to the synthesis temperature for optimized Ni-rich NCM, offering clearer guidance in designing Li-excess Ni-rich NCM materials with advanced electrochemical performance. Based on comprehensive understanding on crystal structure of Ni-rich NCM with different Li content and temperatures, we propose following mechanisms in stabilizing cycling performance of Li-excess NCM via means of synthesis temperature regulation: 1) The Li-excess layered structure is well-formed as the synthesis temperature is lowered, where decreases of Ni^{2+} and increases of Ni^{3+} (mainly) and Ni^{4+} at 800 °C and 750 °C to reduced cation mixing, whereas at 700 °C, decreases of Ni$^{2+/3+}$ and increases of Ni^{4+}, resulting in cation mixing decreases and Li$_2$MO$_3$ is formed. 2) The excess Li can suppress the generation of non-stoichiometric Li$_{1-x}$Ni$_{1+x}$O$_2$ during high-temperature synthesis, Li/Ni cation mixing, and Ni^{2+}O impurity phase formation on the particle surface that degrades Ni-rich NCM properties. 3) Li-excess layered structure formed at 800 °C ~ 750 °C showed stable cycle performances

which can be attributed to the reduced Li/Ni cation mixing and increased immobile Li in the TM layer, whereas Li-excess phase formed at 700 °C exhibited an unstable cycle performance due to the irreversible oxygen redox caused by the activation of Li_2MO_3 phase at a high voltage of 4.5 V [37,38,40].

In practical terms, high energy density (>850 Wh kg^{-1}) and stable cycle performance (91% after 50 cycles) at high voltage can be obtained from Ni-rich NCM without additional cation doping and surface coating processes. Furthermore, controlling the Li content and temperature during the synthesis process in Ni-rich NCM can regulate the degree of Li incorporation in the crystalline lattice and efficiently avoid the formation of residual Li compounds on the particle surface, which requires additional costly washing process. Simple synthetic approach was developed to enhance the electrochemical performance of Ni-rich NCM by going back to the basic process for synthesis, such as Li stoichiometry and synthesis temperature. We believe that our findings will provide a new insight into the synthesis process of Ni-rich layered cathode materials in the industry.

4. Conclusions

In summary, Li-excess Ni-rich NCM materials of $Li_{(1+x)}[Ni_{0.92}Co_{0.04}Mn_{0.04}]_{(1-x)}O_2$ were successfully synthesized, and their crystal and surface structures were characterized using XRD, ND, PDF, and XAS analyses. Our results indicate that excessive Li can be incorporated into the TM layer in a layered structure with a form of $LiMO_2$ (*R-3 m*) or Li_2MO_3 (*C2/m*) by regulating the Li content and synthesis temperature in the course of Ni-rich NCM synthesis. Li-excess samples exhibited low capacity and voltage decay upon repeated battery cycling at a high cut-off voltage of 4.5 V, resulting in superior capacity and energy density retention (91%) after 50 cycles. The electrochemical mechanism was investigated using *in situ* charge/discharge XRD analyses, which indicated that a small lattice change occurred from the Li-excess electrode because immobile Li in the TM layer plays the role of structural stabilizer. This study highlights the importance of heating temperature and Li content in synthesizing Ni-rich NCM materials and provides new insights for the design of Li off-stoichiometric electrodes with stable electrochemical performance under high-voltage operation.

Declaration of Competing Interest

The authors declare that they have no known competing financial interests or personal relationships that could have appeared to influence the work reported in this paper.

Data availability

Data will be made available on request.

Acknowledgements

Appendix A. Supplementary data

Supplementary data to this article can be found online at https://doi. org/10.1016/j.cej.2022.137685.

References

[1] S.-T. Myung, F. Maglia, K.-J. Park, C.S. Yoon, P. Lamp, S.-J. Kim, Y.-K. Sun, Nickel-rich layered cathode materials for automotive lithium-ion batteries: achievements and perspectives, ACS Energy Lett. 2 (2016) 196–223, https://doi.org/10.1021/acsenergylett.6b00594.

[2] A. Manthiram, J.C. Knight, S.T. Myung, S.M. Oh, Y.K. Sun, Nickel-rich and lithium-rich layered oxide cathodes: progress and perspectives, Adv. Energy Mater. 6 (2016) 1501010, https://doi.org/10.1002/aenm.201501010.

[3] H.H. Sun, H.-H. Ryu, U.-H. Kim, J.A. Weeks, A. Heller, Y.-K. Sun, C.B. Mullins, Beyond doping and coating: prospective strategies for stable high-capacity layered Ni-rich cathodes, ACS Energy Lett. 5 (2020) 1136–1146, https://doi.org/10.1021/acsenergylett.0c00191.

[4] A. Rougier, P. Gravereau, C. Delmas, Optimization of the composition of the $Li_{1-z}Ni_{1+z}O_2$ electrode materials: structural, magnetic, and electrochemical studies, J. Electrochem. Soc. 143 (1996) 1168–1175, https://doi.org/10.1149/1.1836614.

[5] C. Pouillerie, E. Suard, C. Delmas, Structural characterization of $Li_{1-z-x}Ni_{1+z}O_2$ by neutron diffraction, J. Solid State Chemistry 158 (2001) 187–197, https://doi.org/10.1006/jssc.2001.9092.

[6] M. Bianchini, M. Roca-Ayats, P. Hartmann, T. Brezesinski, J. Janek, There and back again—the journey of $LiNiO_2$ as a cathode active material, Angew. Chem. Int. Ed. 58 (2019) 10434–10458, https://doi.org/10.1002/anie.201812472.

[7] R. Jung, M. Metzger, F. Maglia, C. Stinner, H.A. Gasteiger, Oxygen release and its effect on the cycling stability of $LiNi_xMn_yCo_zO_2$ (NMC) cathode materials for Li-ion batteries, J. Electrochem. Soc. 164 (2017) A1361–A1377, https://doi.org/10.1149/2.0021707jes.

[8] J. Wandt, A.T. Freiberg, A. Ogrodnik, H.A. Gasteiger, Singlet oxygen evolution from layered transition metal oxide cathode materials and its implications for lithium-ion batteries, Mater. Today 21 (2018) 825–833, https://doi.org/10.1016/j.mattod.2018.03.037.

[9] H.-H. Ryu, K.-J. Park, C.S. Yoon, Y.-K. Sun, Capacity fading of Ni-rich Li $[Ni_xCo_yMn_{1-x-y}]O_2$ ($0.6 \leq x \leq 0.95$) cathodes for high-energy-density lithium-ion batteries: bulk or surface degradation? Chem. Mater. 30 (2018) 1155–1163, https://doi.org/10.1021/acs.chemmater.7b05269.

[10] H.-H. Ryu, G.-T. Park, C.S. Yoon, Y.-K. Sun, Microstructural Degradation of Ni-Rich Li $[Ni_xCo_yMn_{1-x-y}]O_2$ Cathodes During Accelerated Calendar Aging, Small 14 (2018) 1803179, https://doi.org/10.1002/smll.201803179.

[11] Y. Mao, X. Wang, S. Xia, K. Zhang, C. Wei, S. Bak, Z. Shadike, X. Liu, Y. Yang, R. Xu, P. Pianetta, S. Ermon, E. Stavitski, K. Zhao, Z. Xu, F. Lin, X.-Q. Yang, E. Hu, Y. Liu, High-voltage charging-induced strain, heterogeneity, and micro-cracks in secondary particles of a nickel-rich layered cathode material, Adv. Funct. Mater. 29 (2019) 1900247, https://doi.org/10.1002/adfm.201900247.

[12] S.-M. Bak, E. Hu, Y. Zhou, X. Yu, S.D. Senanayake, S.-J. Cho, K.-B. Kim, K.Y. Chung, X.-Q. Yang, K.-W. Nam, Structural changes and thermal stability of charged $LiNi_xMn_yCo_zO_2$ cathode materials studied by combined in situ time-resolved XRD and mass spectroscopy, ACS Appl. Mater. Interfaces 6 (2014) 22594–22601, https://doi.org/10.1021/am506712c.

[13] S.-K. Jung, H. Kim, S.H. Song, S. Lee, J. Kim, K. Kang, Unveiling the role of transition-metal ion in the thermal degradation of layered Ni–Co–Mn cathodes for lithium rechargeable batteries, Adv. Funct. Mater. 2108790 (2021), https://doi.org/10.1002/adfm.202108790.

[14] K. Kang, Y.S. Meng, J. Bréger, C.P. Grey, G. Ceder, Electrodes with high power and high capacity for rechargeable lithium batteries, Science 311 (2006) 977–980, https://doi.org/10.1126/science.1122152.

[15] S.-K. Jung, H. Gwon, J. Hong, K.-Y. Park, D.-H. Seo, H. Kim, J. Hyun, W. Yang, K. Kang, Understanding the degradation mechanisms of LiNi 0.5 Co 0.2 Mn 0.3 O 2 cathode material in lithium ion batteries, Adv. Energy Mater. 4 (1) (2014) 1300787.

[16] S.H. Song, M. Cho, I. Park, J.-G. Yoo, K.-T. Ko, J. Hong, J. Kim, S.-K. Jung, M. Avdeev, S. Ji, S. Lee, J. Bang, H. Kim, High-voltage-driven surface structuring and electrochemical stabilization of Ni-Rich layered cathode materials for Li rechargeable batteries, Adv. Energy Mater. 10 (23) (2020) 2000521.

[17] H.-X. Wei, L.-B. Tang, Y.-D. Huang, Z.-Y. Wang, Y.-H. Luo, Z.-J. He, C. Yan, J. Mao, K.-H. Dai, J.-C. Zheng, Comprehensive understanding of Li/Ni intermixing in layered transition metal oxides, Mater. Today 51 (2021) 365–392, https://doi.org/10.1016/j.mattod.2021.09.013.

[18] J. Zheng, Y. Ye, T. Liu, Y. Xiao, C. Wang, F. Wang, F. Pan, Ni/Li disordering in layered transition metal oxide: electrochemical impact, origin, and control, Acc. Chem. Res. 52 (2019) 2201–2209, https://doi.org/10.1021/acs.accounts.9b00033.

[19] J. Kim, H. Lee, H. Cha, M. Yoon, M. Park, J. Cho, Prospect and reality of Ni-rich cathode for commercialization, Adv. Energy Mater. 8 (2018) 1702028, https://doi.org/10.1002/aenm.201702028.

[20] M. Guilmard, L. Croguennec, C. Delmas, Effects of manganese substitution for nickel on the structural and electrochemical properties of $LiNiO_2$, J. Electrochem. Soc. 150 (2003) A1287–A1293, https://doi.org/10.1021/10.1149/1.1601227.

[21] T. Weigel, F. Schipper, E.M. Erickson, F.A. Susai, B. Markovsky, D. Aurbach, Structural and electrochemical aspects of $LiNi_{0.8}Co_{0.1}Mn_{0.1}O_2$ cathode materials doped by various cations, ACS Energy Lett. 4 (2019) 508–516, https://doi.org/10.1021/acsenergylett.8b02302.

[22] W. Lee, S. Muhammad, T. Kim, H. Kim, E. Lee, M. Jeong, S. Son, J.H. Ryou, W. S. Yoon, New insight into Ni-rich layered structure for next-generation Li

rechargeable batteries, Adv. Energy Mater. 8 (2018) 1701788, https://doi.org/10.1002/aenm.201701788.

[23] U.-H. Kim, G.-T. Park, B.-K. Son, G.W. Nam, J. Liu, L.-Y. Kuo, P. Kaghazchi, C. S. Yoon, Y.-K. Sun, Heuristic solution for achieving long-term cycle stability for Ni-rich layered cathodes at full depth of discharge, Nat. Energy 5 (2020) 860–869, https://doi.org/10.1038/s41560-020-00693-6.

[24] M. Yoon, Y. Dong, J. Hwang, J. Sung, H. Cha, K. Ahn, Y. Huang, S.J. Kang, J. Li, J. Cho, Reactive boride infusion stabilizes Ni-rich cathodes for lithium-ion batteries, Nat. Energy 6 (2021) 362–371, https://doi.org/10.1038/s41560-021-00845-2.

[25] C.-H. Jung, D.-H. Kim, D. Eum, K.-H. Kim, J. Choi, J. Lee, H.-H. Kim, K. Kang, S.-H. Hong, New Insight into Microstructure Engineering of Ni-Rich Layered Oxide Cathode for High Performance Lithium Ion Batteries, Adv. Funct. Mater. 31 (18) (2021) 2010095.

[26] K.-Y. Park, Y. Zhu, C.G. Torres-Castanedo, H.J. Jung, N.S. Luu, O. Kahvecioglu, Y. Yoo, J.-W.-T. Seo, J.R. Downing, H.-D. Lim, M.J. Bedzyk, C. Wolverton, M. C. Hersam, Elucidating and mitigating high-voltage degradation cascades in cobalt-free LiNiO₂ lithium-ion battery cathodes, Adv. Mater. 34 (2022) 2106402, https://doi.org/10.1002/adma.202106402.

[27] Z. Yu, X. Qu, T. Wan, A. Dou, Y. Zhou, X. Peng, M. Su, Y. Liu, D. Chu, Synthesis and mechanism of high structural stability of nickel-rich cathode materials by adjusting Li-excess, ACS Appl. Mater. Interfaces 12 (2020) 40393–40403, https://doi.org/10.1021/acsami.0c12541.

[28] K. Park, B. Choi, Requirement of high lithium content in Ni-rich layered oxide material for Li ion batteries, J. Alloys Compd. 766 (2018) 470–476, https://doi.org/10.1016/j.jallcom.2018.06.135.

[29] X. Li, K. Zhang, S. Wang, M. Wang, F. Jiang, Y. Liu, Y. Huang, J. Zheng, Optimal synthetic conditions for a novel and high performance Ni-rich cathode material of LiNi₀.₆₈Co₀.₁₀Mn₀.₂₂O₂, Sustain. Energy Fuels 2 2 (8) (2018) 1772–1780.

[30] C. Zhang, S. Xu, B. Han, G. Lin, Q. Huang, D.G. Ivey, C. Yang, P. Wang, W. Wei, Towards rational design of high performance Ni-rich layered oxide cathodes: the interplay of borate-doping and excess lithium, J. Power Sources 431 (2019) 40–47, https://doi.org/10.1016/j.jpowsour.2019.05.048.

[31] E.B. Abebe, C.-C. Yang, S.-H. Wu, W.-C. Chien, Y.-J.-J. Li, Effect of Li excess on electrochemical performance of Ni-Rich LiNi₀.₉Co₀.₀₅Mn₀.₀₅O₂ cathode materials for Li-ion batteries, ACS Appl. Energy Mater. 4 (2021) 14295–14308, https://doi.org/10.1021/acsaem.1c03004.

[32] C.P. Grey, W.-S. Yoon, J. Reed, G. Ceder, Electrochemical activity of Li in the transition-metal sites of O3 Li[Li₍₁₋₂ₓ₎/₃Mn₍₂₋ₓ₎/₃Niₓ]O₂, Electrochem. Solid-State Lett. 7 (2004) A290, https://doi.org/10.1149/1.1783113.

[33] Y. Liu, Y. Gao, A. Dou, Influence of Li content on the structure and electrochemical performance of Li₁₊ₓNi₀.₂₅Mn₀.₇₅O₂.₂₅₊ₓ/₂ cathode for Li-ion battery, J. Power Sources 248 (2014) 679–684, https://doi.org/10.1016/j.jpowsour.2013.10.006.

[34] S.-T. Myung, S. Komaba, K. Kurihara, K. Hosoya, N. Kumagai, Y.-K. Sun, I. Nakai, M. Yonemura, T. Kamiyama, Synthesis of Li[(Ni₀.₅Mn₀.₅)₁₋ₓLiₓ]O₂ by emulsion drying method and impact of excess Li on structural and electrochemical properties, Chem. Mater. 18 (2006) 1658–1666, https://doi.org/10.1021/cm052704j.

[35] D.-H. Seo, J. Lee, A. Urban, R. Malik, S. Kang, G. Ceder, The structural and chemical origin of the oxygen redox activity in layered and cation-disordered Li-excess cathode materials, Nat. Chem. 8 (2016) 692–697, https://doi.org/10.1038/nchem.2524.

[36] W.E. Gent, K. Lim, Y. Liang, Q. Li, T. Barnes, S.-J. Ahn, K.H. Stone, M. McIntire, J. Hong, J.H. Song, Y. Li, A. Mehta, S. Ermon, T. Tyliszczak, D. Kilcoyne, D. Vine, J.-H. Park, S.-K. Doo, M.F. Toney, W. Yang, D. Prendergast, W.C. Chueh, Coupling between oxygen redox and cation migration explains unusual electrochemistry in lithium-rich layered oxides, Nat. Commun. 8 (2017) 1–12, https://doi.org/10.1038/s41467-017-02041-x.

[37] K. Ku, J. Hong, H. Kim, H. Park, W.M. Seong, S.-K. Jung, G. Yoon, K.-Y. Park, H. Kim, K. Kang, Suppression of voltage decay through manganese deactivation and nickel redox buffering in high-energy layered lithium-rich electrodes, Adv. Energy Mater. 8 (2018) 1800606, https://doi.org/10.1002/aenm.201800606.

[38] M. Tabuchi, N. Kuriyama, K. Takamori, Y. Imanari, K. Nakane, Appearance of lithium-excess LiNiO₂ with high cyclability synthesized by thermal decomposition route from LiNiO₂-Li₂NiO₃ solid solution, J. Electrochem. Soc. 163 (10) (2016) A2312–A2317, https://doi.org/10.1149/2.0861610jes.

[39] P. Kurzhals, F. Riewald, M. Bianchini, H. Sommer, H.A. Gasteiger, J. Janek, The LiNiO₂ cathode active material: a comprehensive study of calcination conditions and their correlation with physicochemical properties. Part I. Structural chemistry, J. Electrochem. Soc. 168 (11) (2021) 110518, https://doi.org/10.1149/1945-7111/ac33e5.

[40] M. Bianchini, A. Schiele, S. Schweidler, S. Sicolo, F. Fauth, E. Suard, S. Indris, A. Mazilkin, P. Nagel, S. Schuppler, M. Merz, P. Hartmann, T. Brezesinski, J. Janek, From LiNiO₂ to Li₂NiO₃: synthesis, structures and electrochemical mechanisms in Li-Rich nickel oxides, Chem. Mater. 32 (21) (2020) 9211–9227.

[41] W.M. Seong, K.H. Cho, J.W. Park, H. Park, D. Eum, M.H. Lee, I.s.S. Kim, J. Lim, K. Kang, Controlling residual lithium in high-nickel (> 90%) lithium layered oxides for cathodes in lithium-ion batteries, Angew. Chem. Int. Ed. 59 (2020) 18662–18669, https://doi.org/10.1002/anie.202007436.

[42] L. You, B. Chu, G. Li, T. Huang, A. Yu, H₃BO₃ washed LiNi₀.₈Co₀.₁Mn₀.₁O₂ with enhanced electrochemical performance and storage characteristics, J. Power Sources 482 482 (2021) 228940.

[43] C.L. Farrow, P. Juhas, J.W. Liu, D. Bryndin, E.S. Božin, J. Bloch, T.h. Proffen, S.J. L. Billinge, PDFfit2 and PDFgui: computer programs for studying nanostructure in crystals, J. Condens. Matter Phys. 19 (33) (2007) 335219, https://doi.org/10.1088/0953-8984/19/33/335219.

[44] J. Zhao, W. Zhang, A. Huq, S.T. Misture, B. Zhang, S. Guo, L. Wu, Y. Zhu, Z. Chen, K. Amine, F. Pan, J. Bai, F. Wang, In situ probing and synthetic control of cationic ordering in Ni-Rich layered oxide cathodes, Adv. Energy Mater. 7 (3) (2017) 1601266, https://doi.org/10.1002/aenm.201601266.

[45] M. Dixit, B. Markovsky, F. Schipper, D. Aurbach, D.T. Major, Origin of structural degradation during cycling and low thermal stability of Ni-rich layered transition metal-based electrode materials, J. Phys. Chem. C 121 (2017) 22628–22636, https://doi.org/10.1021/acs.jpcc.7b06122.

[46] M.-J. Zhang, G. Teng, Y.-C.-K. Chen-Wiegart, Y. Duan, J.Y.P. Ko, J. Zheng, J. Thieme, E. Dooryhee, Z. Chen, J. Bai, K. Amine, F. Pan, F. Wang, J. Am. Chem. Soc. 140 (2018) 12484–12492, https://doi.org/10.1021/jacs.8b06150.

[47] M. Guilmard, A. Rougier, M. Grüne, L. Croguennec, C. Delmas, Effects of aluminum on the structural and electrochemical properties of LiNiO₂, J. Power Sources 115 (2003) 305–314, https://doi.org/10.1016/S0378-7753(03)00012-0.

[48] K.W. Nam, S.M. Bak, E. Hu, X. Yu, Y. Zhou, X. Wang, L. Wu, Y. Zhu, K.Y. Chung, X. Q. Yang, Combining in situ synchrotron X-ray diffraction and absorption techniques with transmission electron microscopy to study the origin of thermal instability in overcharged cathode materials for lithium-ion batteries, Adv. Funct. Mater. 23 (2013) 1047–1063, https://doi.org/10.1002/adfm.201200693.

[49] N. Palina, L. Wang, S. Dash, X. Yu, M.B. Breese, J. Wang, A. Rusydi, Investigation of the metal–insulator transition in NdNiO₃ films by site-selective X-ray absorption spectroscopy, Nanoscale 9 (2017) 6094–6102, https://doi.org/10.1039/C7NR00742F.

[50] L. Mu, X.u. Feng, R. Kou, Y. Zhang, H. Guo, C. Tian, C.-J. Sun, X.-W. Du, D. Nordlund, H.L. Xin, F. Lin, Deciphering the cathode-electrolyte interfacial chemistry in sodium layered cathode materials, Adv. Energy Mater. 8 (34) (2018) 1801975.

[51] Y. Su, G. Chen, L. Chen, L. Li, C. Li, R. Ding, J. Liu, Z. Lv, Y. Lu, L. Bao, G. Tan, S. Chen, F. Wu, Clean the Ni-Rich cathode material surface with boric acid to improve its storage performance, Front. Chem. 8 (2020) 573, https://doi.org/10.3389/fchem.2020.00573.

[52] H.-H. Sun, A. Manthiram, Impact of microcrack generation and surface degradation on a nickel-rich layered Li[Ni₀.₉Co₀.₀₅Mn₀.₀₅]O₂ cathode for lithium-ion batteries, Chem. Mater. 29 (2017) 8486–8493, https://doi.org/10.1021/acs.chemmater.7b03268.

[53] W. Li, J. Reimers, J. Dahn, In situ x-ray diffraction and electrochemical studies of Li₁₋ₓNiO₂, Solid State Ion. 67 (1993) 123–130, https://doi.org/10.1016/0167-2738(93)90317-V.